

ARTICLE

Received 25 Aug 2014 | Accepted 20 Feb 2015 | Published 27 Mar 2015

DOI: 10.1038/ncomms7712

# Cracks in Martian boulders exhibit preferred orientations that point to solar-induced thermal stress

Martha-Cary Eppes<sup>1</sup>, Andrew Willis<sup>2</sup>, Jamie Molaro<sup>3</sup>, Stephen Abernathy<sup>1</sup> & Beibei Zhou<sup>2</sup>

The origins of fractures in Martian boulders are unknown. Here, using Mars Exploration Rover 3D data products, we obtain orientation measurements for 1,857 cracks visible in 1,573 rocks along the Spirit traverse and find that Mars rock cracks are oriented in statistically preferred directions similar to those compiled herein for Earth rock cracks found in mid-latitude deserts. We suggest that Martian directional cracking occurs due to the preferential propagation of microfractures favourably oriented with respect to repeating geometries of diurnal peaks in sun-induced thermal stresses. A numerical model modified here with Mars parameters supports this hypothesis both with respect to the overall magnitude of stresses as well as to the times of day at which the stresses peak. These data provide the first direct field and numerical evidence that insolation-related thermal stress potentially plays a principle role in cracking rocks on portions of the Martian surface.

<sup>1</sup>Department of Geography and Earth Sciences, University of North Carolina at Charlotte, Charlotte, North Carolina 28223, USA. <sup>2</sup>Department of Electrical and Computing Engineering, University of North Carolina at Charlotte, Charlotte North Carolina 28223, USA. <sup>3</sup>Lunar and Planetary Laboratory, University of Arizona, Tucson, Arizona 85721, USA. Correspondence and requests for materials should be addressed to M.-C.E. (email: meppes@uncc.edu).

Physical weathering is the primary, non-tectonic mechanism for the mechanical breakdown of rock into smaller particles. On Mars, as on Earth, mechanical weathering is the precursor to sediment production and rock erosion, see, for example, refs 1–4, and can potentially influence chemical weathering and subsequent atmospheric feedbacks<sup>5–8</sup>. Hence, identifying the key drivers of weathering is therefore possibly tantamount to understanding the key drivers of landscape change on the Martian surface.

Rocks found in the Mars Exploration Rover (MER) images of the Martian surface commonly exhibit fractures that are visible without magnification (hereafter: ‘cracks’; Fig. 1). In general, Mars cracks have similar characteristics to those observed in rocks found in Earth’s deserts<sup>9–11</sup>. Various hypotheses have been proposed to explain non-Earth mechanical weathering, including damage by original ejecta emplacement<sup>3</sup>, salt weathering<sup>2,10,12</sup> and thermal stress<sup>13–16</sup>. To date, however, no one has collected mechanical weathering data from extraterrestrial rocks themselves that might support, refute or quantify the relative importance of these processes.

Numerical modelling, field data and rock instrumentation convincingly target solar-induced thermal stress as a key mechanism responsible for physical weathering on Earth<sup>17–21</sup>. In particular, a majority of non-bedrock boulders found in Earth’s mid-latitude deserts exhibit cracks with strongly preferred, roughly north–north-east orientations (Fig. 2), even when rock anisotropies such as bedding or foliation are taken into account<sup>22–25</sup>. These orientations are hypothesized to result from Earth’s rotation<sup>22,25</sup>, a geometric relationship which imparts cyclically occurring maximum thermal stresses<sup>26</sup> on boulders as they are directionally heated and cooled during the sun’s daily east-to-west transit across the sky. Although other non-tectonic sources of fracture-inducing rock stress, such as freezing or salt precipitation, may also play a role in fracturing overall, these sources of stress by themselves should produce random crack orientations without the influence of the sun. It is unknown if rocks in other Earth deserts or in other celestial bodies exhibit preferred crack orientations.

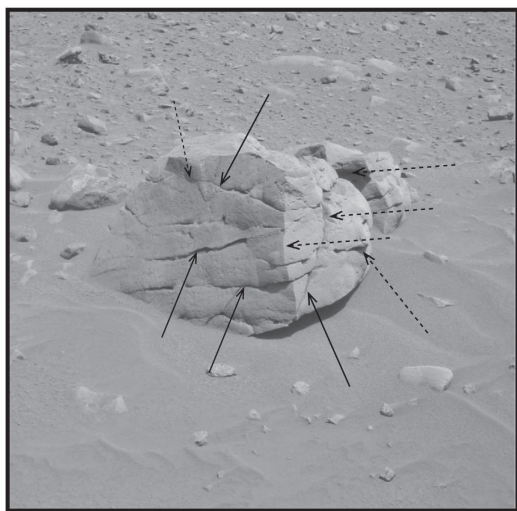


**Figure 1 | Cracked rock on Mars.** Example of a MER Spirit PANCAM image (data product 2p130443923eff0900p255517m1.img, Courtesy NASA/JPL-Caltech Planetary Data System) of a rock with visible cracks from the Martian surface. Image azimuth: 292°. Local True Solar Time: 10:45:08. Sol 46. Site 9. Solid arrows point to linear features that would meet our criteria for a crack (Methods). Dashed arrows point to features such as edges or wide voids that would not meet our criteria for a crack.

Long-term orbital cycles on Mars are thought to be roughly analogous to those of Earth’s Milankovitch cycles<sup>27</sup>. Although the Martian year is about 1.8 times as long as an Earth year, the Martian sidereal day is only about 40 min longer than that of Earth. Mars’ obliquity, or axial tilt, is centred around roughly the same angle as Earth’s<sup>28</sup>, though known to vary by as much as  $\pm 20^\circ$  more over intermediate timescales ( $\sim 5\text{--}10$  Myr ago). Although obliquity is thought to have varied significantly more and in chaotic ways over longer timescales<sup>29</sup>, addressing how these variations might affect insolation-related cracking is beyond the scope of this paper.

Nevertheless, the overall similarity in geometry of insolation between Earth and Mars leads to the expectation that the resulting geometry of thermal stresses that arise, particularly near the equator where MER rovers are located, are also similar and might result in preferred orientations of cracks, albeit possibly at different angles. Herein, analysis of three-dimensional (3D) reconstructions of stereo pair photographs of the Martian surface and output from a two-dimensional (2D) model of diurnal thermoelastic stresses expected from simple insolation-related deformation reveals that Martian boulders do exhibit cracks with preferred orientations, and that calculated solar-induced thermal stresses for Martian rocks are consistent with solar-driven directional cracking.

## Results

**Identifying sampling bias potential in Spirit data products.** We collected a detailed preliminary data set of rock and crack data (Methods and Supplementary Methods) to characterize potential sampling biases that might arise from making such ‘field’ measurements using MER Spirit PANCAM data products in combination with the ‘ImageRover’ software that we developed and validated (Supplementary Figs 1 and 2; Supplementary Table 1). We identified three important data set biases: (1) due to their visibility, cracks observed on Mars will be from relatively larger rocks (Supplementary Data set 1) compared with the data set derived from Earth rocks (Supplementary Data set 2); (2) images collected by the Spirit Rover were disproportionately collected with the PANCAM pointing parallel to the direction of rover motion (NW–SE; Fig. 3). Consequently, the azimuths of randomly chosen images such as those in this preliminary analysis reflect this directional predilection (Fig. 4a); and (3) because of the overall lower visibility of image-parallel-striking cracks in 2D MER images (Methods), the majority of cracks measured in

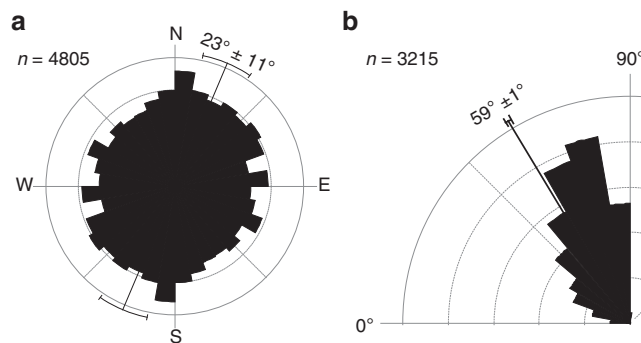


**Figure 2 | Earth crack data compilation.** Data compiled for this paper from other studies of Earth rock cracks in northern, and to a lesser extent southern, hemisphere, mid-latitude deserts (Methods and Supplementary Data set 2)<sup>22–25,62</sup>. Lines point to data vector mean with 95% confidence interval depicted by brackets. Data are plotted in  $10^\circ$  bins with frequency reported in %. (a) Circular bidirectional histogram of crack strike orientations. Raleigh test  $P$  value  $< 0.01$ . Rao’s spacing test  $P$  value  $< 0.01$ . (b) Circular histogram of dip angles from the same cracks where available.

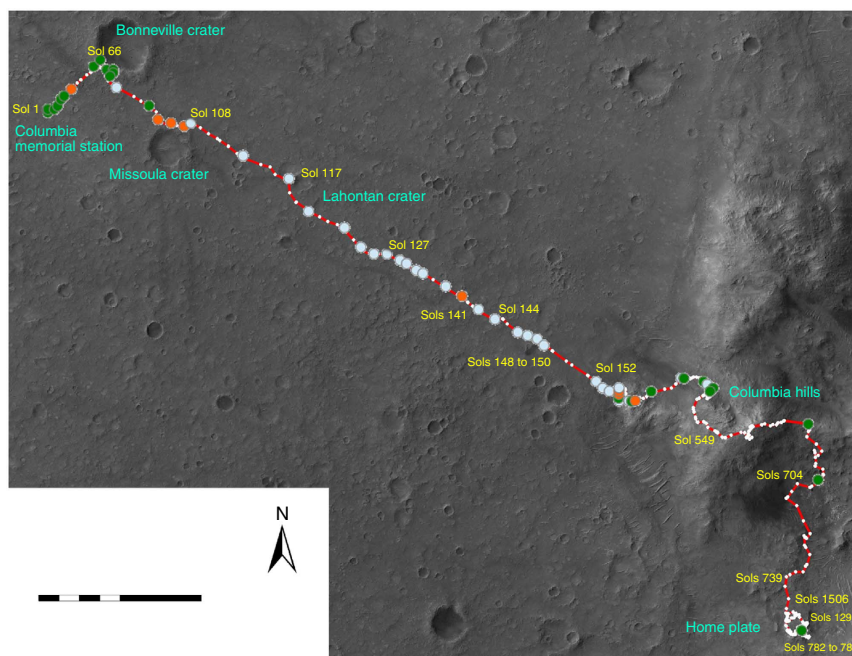


**Figure 3 | Location map.** Sites used for data collection for this study are marked on a map of the Spirit Traverse modified from an image by Ohio State University Mapping and GIS Laboratory<sup>67</sup> provided courtesy of NASA/JPL-CalTech Planetary Data System. The red lines and small white dots represent the path of the Spirit rover and its location by Sol. Larger light blue dots are located at sites where data were collected for the 133-rock data set (Supplementary Data set 1). Green dots are located at sites where data were collected for the 1,440-rock data set (Supplementary Data set 3). Orange dots are located at sites where data were collected for both data sets. Prominent Mars surface features are indicated by name on the map. Scale bar is 1,000 m.

any given image will be striking into, and out of, the photograph. Consequently, there is a strong correlation ( $R^2 = 0.7$ , Pearson  $r = 0.9$ ,  $P$  value  $\leq 0.01$ ) between image azimuth and measured crack strike (Fig. 4b); the difference between image azimuth and measured crack strike was normally distributed about a mean of  $1.7 \pm 27^\circ$  (Fig. 4c).

Crack strike data measured for this preliminary analysis (Fig. 4d,e) therefore share the MER database NW–SE sampling bias of the images themselves (Fig. 4a) and cannot be considered in the context of weathering as sampled. Furthermore, because of the likely obscuration of a larger proportion of vertical to subvertical cracks compared with lower dip cracks (Methods), dip angles measured from this randomly chosen population of images are also therefore likely of a lower-angle on average compared with the actual population. The vector mean and 95% confidence interval of measured Mars crack dip angles was  $39 \pm 3^\circ$  (Fig. 4f and Supplementary Data set 1).

Nevertheless, crack dip direction measured from MER data should not be subject to visual bias. For example west- versus east-dipping cracks should be equally visible in a north–south-oriented photo. Although the time of the day might produce shadows in one direction over another, the images employed were obtained during mid-day hours (Local True Solar Time) with relatively high sun angles (Supplementary Data set 1), precluding bias due to preferential shadowing.

Dip directions observed in Mars rock cracks, as indicated by strikes collected with right-hand rule, were dominantly oriented to the north (75% of all dips; Fig. 4e). This promising result combined with our understanding of sampling biases of the Spirit database led us to the development of a crack measurement method, which would allow us to confidently examine the orientation of crack strikes for Martian rocks.

**Martian rock crack strike orientation analysis.** To accurately record rock crack strikes on the Martian surface, we employed a

stratified sampling strategy to carefully mitigate effects due to observed sampling biases associated with rover traverse direction and crack visibility. Using randomly selected images whose azimuths fell within each of every  $10^\circ$  bin between 0 and  $360^\circ$ , we randomly selected 40 rocks, all  $>20$  cm in maximum ImageRover-measured diameter (Methods; Supplementary Fig. 3). In all, we selected 1,440 rocks (40 rocks from each of 36 bins) located in 31 different sites along the Spirit traverse (Fig. 3; Supplementary Data set 3). Thus, the azimuths of the images for each of the 1,440 selected rocks are equally distributed around  $360^\circ$  (Fig. 5a,b), and this uniform distribution is statistically supported (Raleigh  $P$  value = 0.995; unity on a quantile–quantile plot in Fig. 5c). Both statistical tests are for the null hypothesis of uniformity, with Rao’s testing for multiple modes and Rayleigh testing for a single mode. Because, as described above, crack strikes measured with ImageRover were found to almost equal the image azimuths in which they are found (Fig. 4), we asserted that all visible cracks in the 1,440 rocks will have strikes whose distribution is also normal and equal to that of image azimuths. Thus, if crack orientations on the Martian surface are random in all rocks, then the total numbers of visible cracks should be roughly equal in each of the 36 bins of data, and their overall distribution should mimic the uniform distribution of the image azimuths themselves.

We counted all visible cracks in each of the 1,440 rocks, and 1,635 cracks were observed in 875 rocks (Supplementary Data set 3). Overall, rocks exhibit about one crack per rock; however, this number is likely significantly smaller than the actual average given likely crack visibility limitations for MER images (Supplementary Methods). For each of the 1,635 cracks counted, we assigned it an orientation equal to that of its image azimuth (Fig. 6 and Supplementary Data set 3) to test if the numbers of visible cracks were uniformly distributed about  $360^\circ$ , as would be expected if crack orientations are random.

In the 1,440-rock data set, circular histograms and a quantile–quantile plot of the orientations of cracks reveals a non-uniform,

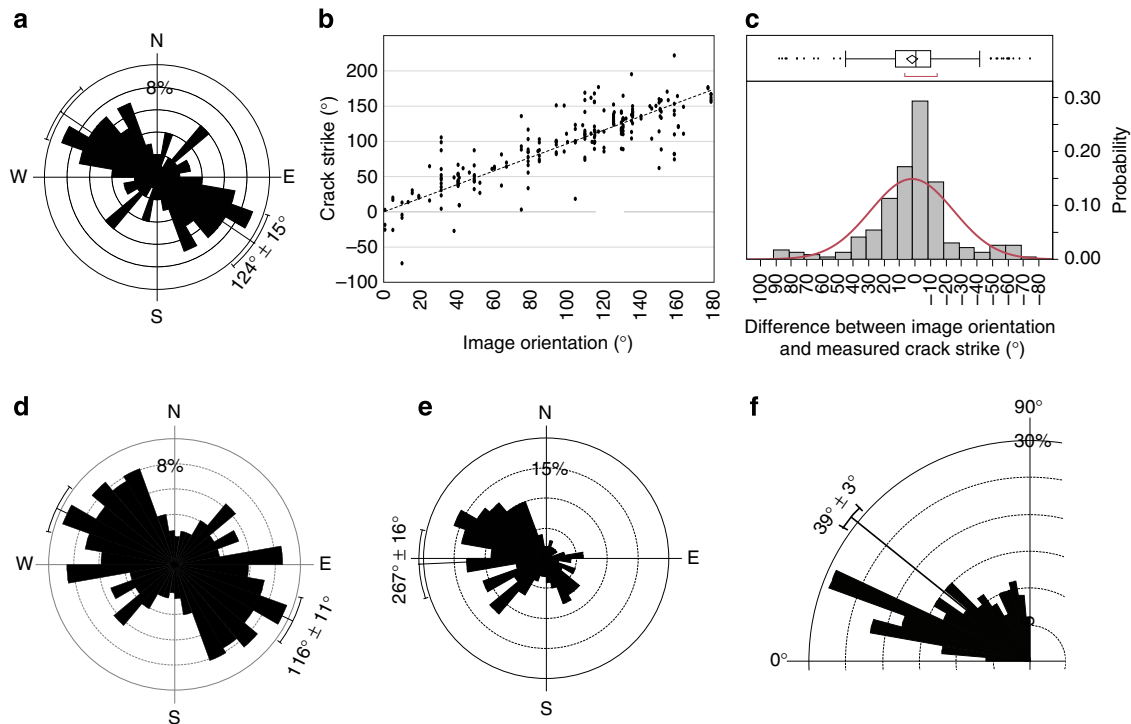


**Figure 4 | 133-Rock data set.** Graphs depicting orientation data collected using ImageRover for 133 rocks and their associated images and cracks. Lines and arcs on circular histograms indicate vector means and associated 95% confidence intervals. Circular histogram data are plotted in  $10^\circ$  bins with frequency reported in %. **(a)** Bidirectionally plotted circular histogram of the orientations of the random selection of images in which the cracks were measured ( $n = 76$ ). **(b)** Graph showing the strong correlation between camera orientations and measured crack strike orientations ( $n = 222$ ;  $y = 0.9672x$ ; Pearson  $r = 0.85$ ; Pearson  $P$  value  $\leq 0.01$ ;  $R^2 = 0.71$ ). **(c)** Histogram, normal fit curve (red line) and box and whisker plot (diamond, mean; vertical line, median; red bracket, densest 50% of data; dots, outliers) of the difference between measured crack strike orientations and their associated image orientations ( $n = 222$ ). **(d)** Bidirectionally plotted circular histogram of the strikes of the cracks ( $n = 222$ ) measured directly from the 133 rocks using ImageRover. **(e)** Unidirectionally plotted circular histogram depicting same data as **b**. Because all crack strikes were measured using the right-hand rule, this graph indicates that measured cracks dip primarily to the northeast. **(f)** Unidirectionally plotted circular histogram depicting the dip angles measured for the cracks ( $n = 222$ ).

preferred distribution of Mars rock crack strikes (Fig. 6a–c). The vector mean and 95% confidence interval for all 1,635 cracks is  $46 \pm 20^\circ$  with a Rayleigh  $P$  value of 0.018 and Rao's spacing test  $P$  value of  $< 0.01$ .

To ensure that this preferred distribution was not related in some way to the visibility of cracks in the afternoon, given the slight preference towards afternoon time stamps in images of the entire data set (average time stamp =  $13:15 \pm 1$  h 35 min), we subsampled the 1,440-rock data set for 360 rocks (10 randomly selected rocks for each of the 36 bins from 0 to 360) to create a subset of rock images with an average time stamp of  $\sim 11:15 \pm 1$  h, 7 min (Supplementary Methods). The vector mean orientation of cracks from this morning-derived subset of images was within  $10^\circ$  of that of the entire population and was also statistically non-random (Supplementary Fig. 4) suggesting no significant difference in crack visibility due to time of day that the image was taken within the range of the mid-day hours of our data set.

We also examined the orientations of images for the 40% of the 1,440 Martian rocks that exhibited no visible cracks with the idea that, if the majority of cracks are preferentially aligned then there are necessarily fewer cracks in other orientations. Since visible cracks share the orientations of images in which they are found, it would therefore be predicted that rocks would be more likely to have zero cracks in image orientations, relative to the viewer, roughly normal to those of the observed majority of cracks. As before, because the azimuths of the images for the 1,440 rocks are equally distributed about  $360^\circ$ , if there is no preference, then the

images associated with rocks with zero cracks should also be randomly distributed around  $360^\circ$ .

The image azimuths for the rocks with no cracks were found to have a preferred direction that was  $75^\circ$  offset from that of visible cracks (vector mean and 95% confidence interval:  $121 \pm 38^\circ$ ; Fig. 6d). Therefore, the implication of this result is that, relative to the viewer, there are in fact fewer visible cracks overall in the NW–SE directions, and thus fewer cracks striking in those directions, as would be predicted given that a majority of Martian rock cracks strike NE–SW. To ensure that cracks with NW–SE orientations are not less visible in afternoon hours, we also analysed the 360-rock morning-only subset of images for rocks with zero cracks. For this subset of data, the NW mode is still evident and prominent (Supplementary Fig. 4). Thus overall, these 'zero crack' data provide additional support for the major finding of our work, which is that cracks in rocks on the Martian surface are statistically non-uniform in their orientations.

### Rock cracking and solar-induced thermal stresses on Mars.

Fracture mechanics dictates that rocks will crack catastrophically when the applied stress exceeds a material-dependent critical threshold (for example, tensile strength, critical energy release rate of Griffith and so on<sup>30</sup>). Single cycles of rapid temperature change are known to exert such stresses on rocks and to cause cracking (thermal shock). Such thermal shock-related cracking is recognized to sometimes result in a tell-tale polygonal pattern of cracking, see, for example, ref. 17. Numerical models<sup>13,15</sup> indicate

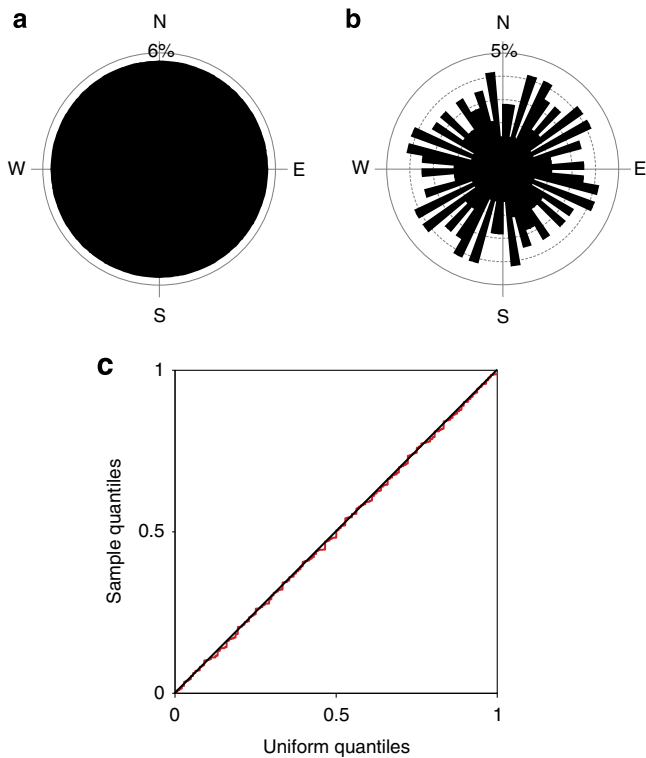


**Figure 5 | Image azimuths 1,440-rock data set.** Graphs of data derived from the orientations of images associated with each of the rocks in which cracks were counted ( $n=1,440$ ). These graphs and their data visually and statistically demonstrate that the selected rock data set removes the image-direction sampling bias associated with MER traverse direction through stratified sampling of images whose azimuths occur in each of 36  $10^\circ$  bins. Frequency data are plotted as percentages. **(a)** Bidirectionally plotted circular histogram of image orientations, plotted in  $10^\circ$  bins ( $n=1,440$  Raleigh test  $P$  value = 0.995.). **(b)** Bidirectionally plotted circular histogram of image orientations, plotted in  $5^\circ$  bins ( $n=1,440$  Raleigh test  $P$  value = 0.995.) **(c)** Quantile-quantile plot of image orientations ( $n=1,440$ ). Black line represents a perfectly uniform distribution. Red line is plotted from image azimuth data.

that terrestrial-body (including Mars) rates of solar-induced rock surface temperature change are as fast as those hypothesized to lead to thermal shock, and polygonal cracking is observed in some MER images of bedrock, see, for example, ref. 2; however, we did not commonly observe these crack patterns in Martian boulders.

It is well established, however, that all rocks are characterized by flaws such as grain boundaries or pores that will act as foci for stresses and thus for crack propagation, see, for example, ref. 31. Such flaws can develop into cracks that slowly and predictably propagate via subcritical crack growth at stresses much lower (the limit is not well defined but is often cited as  $\sim 20\%$  of the critical value<sup>32</sup>) than a material's critical threshold.

There is evidence to suggest that such processes contribute to mechanical weathering of rocks on Mars. For thermal stress cycles associated with diurnal insolation, subcritical crack growth can be facilitated by fatigue, whereby cyclic loading serves to preferentially weaken the material at crack tips and result in crack lengthening and rock degradation, see, for example, ref. 20. These thermally driven cracking processes are undeniably complicated and likely influenced by factors ranging from mineral axis thermal anisotropies, see, for example, ref. 33, to mineral translucence<sup>34,35</sup>, to edge effects. Nevertheless, laboratory experiments produce thermal fatigue-related fracturing when

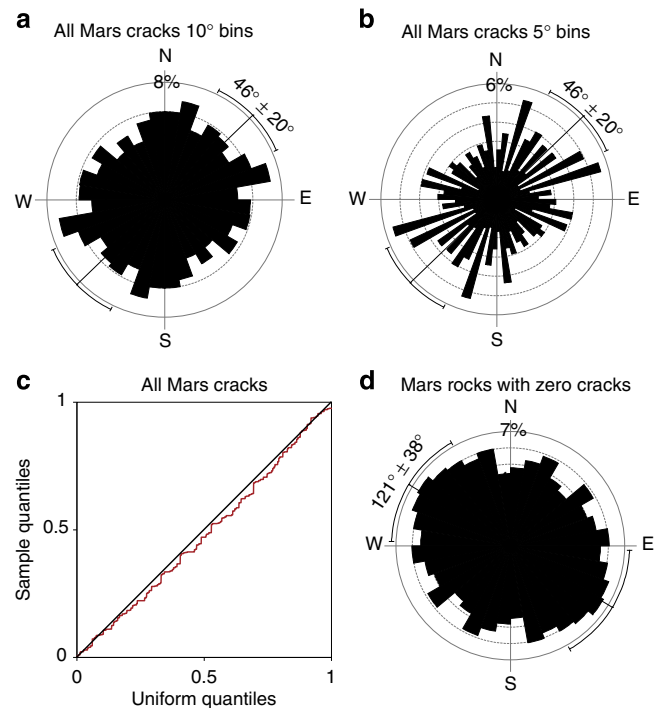


**Figure 6 | Mars rock-crack data analysis.** Graphs of crack data derived from 1,440 rocks selected along the MER Spirit traverse indicating that cracks exhibit preferred orientations. Lines and arcs on circular histograms indicate vector means and associated 95% confidence intervals. Frequencies are reported in %. Bidirectionally plotted circular histogram of the strikes of all visible cracks, plotted in **(a)**  $10^\circ$  and **(b)**  $5^\circ$  bins ( $n=1,635$ ; Rayleigh test  $P$  value = 0.018 and Rao's spacing test  $P$  value  $< 0.01$ ). **(c)** A quantile-quantile plot of the same data as **a**. Black line represents a perfectly uniform distribution. Red line is plotted from image azimuth data. Divergence of the plot of cracks with the 1:1 line indicates preferred orientations. **(d)** Bidirectionally plotted circular histogram of image orientations for rocks that exhibited no cracks, plotted in  $10^\circ$  bins ( $n=565$ ; Raleigh test  $P$  value = 0.35; Rao's spacing test  $P$  value  $< 0.01$ ).

subjecting basalts to thermal cycling replicating Mars temperature extremes<sup>16</sup>. Furthermore, numerical models of solar-induced thermal stresses on Earth<sup>36</sup> and other planetary bodies<sup>37</sup> are well within the range of stresses expected to produce subcritical crack growth, and in some cases exceed the reported critical rock strength values of most rock types. Such stresses have not been calculated for the Mars surface.

Here we use a previously developed 2D finite-element model<sup>38,39</sup> of the thermoelastic behaviour of rock microstructures (small sections of an infinite half-space) subjected to diurnal thermal forcing to simulate, for the first time, solar-induced thermal stresses that might develop on a polycrystalline rock (Supplementary Table 2) on the Martian surface, and determine if such stresses may be sufficient to induce crack propagation (Methods). The microstructures have properties typical of basalt, a common rock type abundant along the MER Spirit traverse.

The surface temperature of a microstructure at a longitude of  $0^\circ$  and the latitude of the Spirit traverse ( $15^\circ\text{S}$ ) was calculated over one solar day on the warmest day of the year ( $L_s$  68) at that location. We calculate that rock surface temperature varies on this day from 186 to 192 K (Fig. 7). This range is substantially smaller than many reported values for Martian surface temperatures (up to 120 K, see, for example, ref. 40). Nevertheless this small

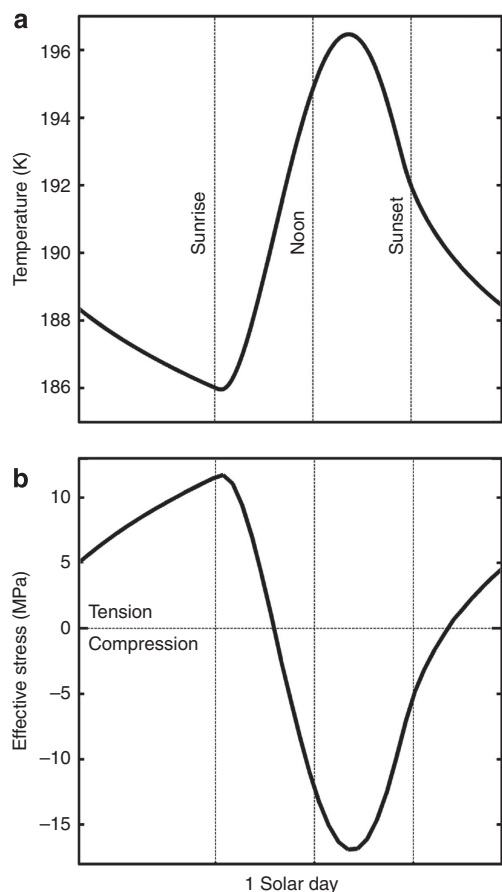


**Figure 7 | Numerical model results.** Results from our modification of a pre-existing model<sup>38</sup> to calculate solar-induced thermal stresses arising in the surface of a subaerially exposed Martian rock (see Methods for details). **(a)** Surface temperatures calculated over one solar day for a microstructure found in an idealized basalt located at a longitude of 0° and the latitude (15°S) of the Spirit traverse. **(b)** Calculated thermoelastic stresses induced within the microstructure throughout the solar day for the same rock using the temperatures derived for **a** above as inputs.

temperature range is consistent with THEMIS data, which shows decreasing range in temperature with increasing thermal inertia<sup>41</sup>. Bedrock has a higher thermal conductivity than unconsolidated sediment, resulting in four to five times higher thermal inertia<sup>42,43</sup>. Also, the thinner Martian atmosphere will serve to dampen diurnal warming effects compared with those of Earth. Although our calculated values represent an annual maxima<sup>38</sup>, these diurnal temperature ranges calculated for a large slab are also likely lower than those which might arise in an individual, relatively small boulder, which will heat up more than flat ground due to its size and the influence of radiation from surrounding terrain.

The thermoelastic stresses induced within the microstructure throughout the solar day are also calculated (Methods). These stresses peak in the tensile regime at 12 MPa, and at 17 MPa in the compressional regime. These values represent the amount of idealized energy available for crack propagation, as the model does not account for the release of mechanical energy as propagation occurs.

Our modelling indicates that the magnitude of stress induced by solar-forcing within the microstructure is primarily controlled by rock surface temperature diurnal range and the Young's modulus and coefficient of thermal expansion of component mineral types<sup>38,39</sup>. This dependence is consistent with other types

of models developed for solar-induced thermal stresses in rocks on Earth, see, for example, ref. 36.

Molaro *et al.*<sup>38</sup> found that bodies close to the Sun and bodies that rotate slowly have the largest daily temperature ranges and thus highest stresses. Earth and Mars have nearly the same rotation rates; however, due to its closer proximity to the Sun, Earth is expected to have a larger diurnal temperature range. Maximum diurnal rock surface temperature fluctuations measured in a variety of climates and latitudes on Earth range from ~20 to ~60 °C, see, for example, ref. 44 and are therefore consistent with this prediction from our model. Consequently, rocks on Earth likely experience higher solar-induced microstructure stresses than on Mars and rock lifetimes on the two planets support this conclusion (see below). In addition, the strength of the materials in vacuum can be one to several times higher than in atmosphere<sup>45</sup>; thus, even comparable stresses between the two bodies may result in faster breakdown rates on Earth.

Similar modelling of grain-scale diurnal thermal stresses has not been completed for Earth. Nevertheless, calculations of maximum solar-induced macroscopic thermal stresses arising in Earth boulders yield values on the order of those calculated herein<sup>26,36</sup>. Because these macroscopic stresses would be predicted to be lower overall than grain-scale stresses, the other modelling results are consistent with our prediction of higher microstructure stresses for a rock on Earth. How such macrostresses might interact with microstresses to produce rock fractures is currently unknown.

It is non-trivial to relate calculated stresses to actual rock breakdown, as rock strength at the grain scale is generally not a well characterized material property and is dependent on a host of factors. Nonetheless, measurements of rock tensile strengths at larger scales are generally of a similar order of magnitude (10–100 s of MPa, see, for example, ref. 46) to stresses calculated by our model and within the cited 80% limit for subcritical crack growth. However, any given amount of external loading exerted on a large scale will result in more damage than for a small scale due to the former having generally more, and larger, pre-existing cracks, see, for example, ref. 30. Thus, rock strengths at grain scales are likely higher than those measured in a hand sample. However, the magnitudes of our modelled stresses likely represent a minimum since our model does not account for pre-existing defects, which will serve to amplify stresses, see, for example, ref. 45. Thus, we conclude that the results of our numerical model, at a minimum, are consistent with the suggestion that thermal stresses arising from simple diurnal insolation are sufficient to drive subcritical, fatigue-driven fracture growth in Martian rocks.

**Linking macrocrack orientation and insolation.** We hypothesize that cracks on Mars exhibit preferred orientations because the geometry of directional heating by the sun drives fatigue-related cracking in preferred directions. Both critical- and subcritical-fracture propagation direction in solid materials is strongly linked to the direction of the applied stress, see, for example, refs 30,47. In a rock with randomly oriented microfractures or zones of weakness (for example, different sides of an individual crystal grain), those heterogeneities whose orientations are favourable with respect to the orientation of the external loading will preferentially propagate and coalesce relative to cracks with other less-favourable orientations, see, for example, refs 48,49. Because subsequent fracture will favourably occur in directions where the density of pre-existing cracks is highest<sup>49</sup>, if loading direction is consistent, a positive feedback develops whereby additional cracking is predicted to result in fracturing

along already preferentially weakened planes. Furthermore, it has been explicitly demonstrated through laboratory experiments that directional thermal stress loading in particular can result in the preferential propagation of cracks of specific orientations with respect to the location of the heat source<sup>50</sup>, and models of thermal stress arising in a hollow sphere subject to a rotating heat source indicate that the orientation of stresses are dictated by the orientation of heating<sup>51</sup>. Thus, if solar-induced thermal stresses on Mars are sufficient, as we have shown, to result in fracture propagation in rocks exposed on the Martian surface, it would then be expected that fracture growth would occur preferentially in directions dictated by insolation itself.

Calculated solar-induced, cyclic thermal stresses on Earth and other terrestrial bodies are not diurnally static, but instead peak at particular times of day: sunrise, mid-day or shortly thereafter and sunset<sup>15,26</sup>. Acoustic emission monitoring of cracking in three different  $\sim 25$  cm diameter boulders, placed for multiple years in mid-latitude locations on Earth, indicates that  $>80\%$  of all cracking events occur in the afternoon hours, with frequency peaks at times<sup>18</sup> that are virtually identical to the timing of peak solar-induced thermal stresses calculated using inputs from the rocks themselves<sup>26</sup>.

Because the peak stresses that are driving this cracking are induced by a rotating heat source, they represent directional loading whose average direction should relate to the average sun orientation at those times of day. Assuming that cracks propagate in a direction that is directly related to the direction of external thermal stress loading as explained above, then arises the potential for a majority of cracks in any given rock to be oriented in a range of directions that reflect the orientation of stresses induced by the sun. The higher density of cracks with sun-related orientations could then result in their preferential extension by other processes like salt-shattering. That such preferentially oriented cracks might develop despite these other processes as well as complicating factors, such as mineral anisotropy or translucence at grain scales, suggests that rock-scale stresses related to the geometry of the boulder itself potentially play an important role in their formation.

To date, there is no existing analysis of the orientations of rock-scale stresses that arise during peak-solar-induced-stress times for a boulder sitting on a ground surface. However, high spatial- and temporal-resolution field measurements of rock surface temperatures reveal that there is a distinct gradient and geometry in average boulder surface temperatures that recurs throughout the day and/or year for rocks on Earth exposed to the sun, see, for example, refs 18,52. Furthermore, isotherms (zones of equal temperatures) measured on boulder surfaces on Earth at the times of day when cracking occurs exhibit strongly defined NE orientations<sup>18</sup>. The overall mean and modal orientation(s) of these isotherms is roughly the same as the vector mean of both Earth (Fig. 2) and Mars (Fig. 6) crack strike data.

Given the overall general similarity in geometry of insolation between Earth and Mars along the Spirit traverse, there is no reason to believe that similar isotherms, and thus similarly oriented stresses, would not also develop in Martian rocks. For example, the surface depth of a diurnal-temperature-wave on Earth and Mars are comparable (such 'skin depth' is proportional to the square root of the diurnal period). Even though overall Martian rock surface temperatures will be lower, the portions of a Martian rock in sunlight will still heat up relative to parts of the rock in shadows. We thus expect that specific geometries of peak stresses will recur on Mars as on Earth even if the magnitude of those stresses differs. This analogy leads to the expectation that Martian insolation-driven thermal stresses will also result in preferred propagation of favourably oriented cracks, ultimately resulting in a population of macrocracks with preferred

directions, as we have observed (see, for example, Figs 2a and 6a). We test this hypothesis by determining if peak stresses that arise in Martian rocks also occur at specific times of day.

Our thermoelastic model shows that the magnitude of stresses induced within microstructures on the Martian surface varies throughout the day with distinct peaks (Fig. 7). Peak tensile stresses occur just before sunrise, as the surface continues to radiate heat into space throughout the night, more so than occurs on Earth. Any atmosphere dampens this cooling by reradiating some of that infrared energy back into the surface. Thus, all else being equal, an airless surface would be able to reach a lower temperature than a Martian surface, or in turn Earth's surface. Nevertheless, similar sunrise peaks in calculated tensile stresses also occur for Earth boulders<sup>26</sup>.

Our model's calculated peak compressional stresses on Mars occur in afternoon hours between noon and sunset. At this time of day, atmospheric radiation causes net heating to continue for longer on Mars than it would on an airless body, and thus this peak occurs slightly later on Mars<sup>38,39</sup>. This result suggests that, on Earth, surfaces should experience this peak state even later in the day, a prediction that is supported by observations of rock surface temperatures that peak in the late afternoon, see, for example, ref. 18.

The mid-afternoon timing of peak compressional stresses developing on Mars is similar to those calculated for compressional stresses arising in the surface of a large isotropic rock sphere due to solar-induced thermal cycles on Earth<sup>26</sup>. While compressional stresses are less likely to produce fracture, the Earth model predicts a roughly simultaneously occurring peak in interior tensile stresses as the warm boulder surface pulls away from the relatively cool interior during these hours. Our model does not explicitly calculate interior stresses that may develop in a Martian boulder. However, the similarities between the two models and the similar skin depths between the two planets suggests that Martian interior tensile stresses will peak coincidentally with exterior compressional stresses, in the afternoon hours, as on Earth. Thus overall, the temporal peaks in stresses that our model calculates suggest that Martian rock cracking will also preferentially occur in the mid-afternoon and morning hours.

Our model predicts that a broad, flat Martian rock surface will go back into tension shortly after sunset. However, we expect variability in the timing of this transition and magnitude of tensile stresses when considering boulders, which have different sizes and shapes. Variability in the overall timing of stresses will also arise from the influence of atmospheric radiation; thus, we expect that the times of peak stresses on Earth and Mars to be somewhat different, and to possibly lead to subtle differences in crack orientations.

## Discussion

The strikes of Mars rock cracks along the Spirit traverse strike more easterly with a somewhat greater variance (Fig. 6) than those from our compilation of published strike data derived from 4,805 cracks in rocks from Earth's mid-latitude deserts, whose vector mean and 95% confidence interval is  $23 \pm 11^\circ$  (Raleigh and Rao's  $P$  values  $<0.01$ ; Fig. 2). A 0.003  $P$  value for a circular-data  $\chi^2$ -test<sup>53</sup> indicates that the two populations are statistically distinct. Also, observed Mars crack dip directions (Fig. 4) are opposite those of many observed on Earth<sup>23</sup>, and there is an overall higher prominence of an E-W mode of orientations in the Mars data.

For a variety of reasons, it might be expected that Earth and Mars cracks may differ in crack orientations and variance. For example, the fact that the Mars crack data set was derived from a low-latitude, southern hemisphere location, combined with the

higher angle of average Martian obliquity<sup>29</sup> would lead to the expectation of different angles of insolation and thus thermal stress-driven cracking. Furthermore, in the most general terms, solar-induced thermal stresses that likely arise in any given rock are complex, and the magnitude of the influence of such stress on rock cracking is likely dependent on a host of factors that we do not explicitly address including latitude<sup>44</sup>, topographic shading<sup>13</sup>, rock composition<sup>34,37</sup> and/or rock shape and size<sup>26</sup>. This complexity is highlighted by the fact that calculated maxima in solar-related thermal stresses occur at different times of day for different topographic locations and different size rocks<sup>13,15,26,37</sup>. These complexities also lead to the expectation that dominant crack orientations will vary somewhat with rock size, composition, shape and overall location. We see evidence of this variability in our compilation of Earth field data which shows relatively large variance (Fig. 2) compared with that of individual data sets<sup>23–25</sup>. On Earth, this variance can be explained by the wide variety of landscapes in which these data are derived, as well as by the fact that other mechanical weathering processes are likely active on Earth's surface.

On Mars, it might therefore be expected that such other processes are more limited and thus crack orientations should exhibit less variance; however, there are other mechanical weathering processes likely acting on the Martian surface (for example, wind abrasion, impact shattering) that could introduce variance into the observed Mars crack orientation data. For example, in addition to insolation, wind can also induce rapid rock surface temperature changes on Earth<sup>54</sup>. Strong afternoon-dominant winds are expected from numerical models of the terrain along the Spirit traverse, and mid-day winds have been noted from images of rock cutting dust<sup>55</sup>. Although thermal advection effects are complicated on Mars due to the lower density of its atmosphere, in general surface winds might serve to advect heat off the rock surface at a time of day when thermal stress is already high, amplifying the potential for thermal stress in afternoon hours and increasing variance in potential stress fields that develop.

Furthermore, the range of rock sizes for the Martian data set (20–400 cm) was much higher than that of the Earth data sets (generally <50 cm; Supplementary Data set 2), potentially resulting in greater variance in the times of day when cracking occurs and thus in crack orientations. In particular, sunset-coincident peaks in solar-induced thermal stress are not predicted in Earth-based models for relatively large rocks like those measured here<sup>26</sup>. Instead, calculated peak stresses occur during the early mid-afternoon. Less sunset cracking in the overall larger rocks of the data set might therefore account for the more easterly orientation of the Mars data set compared with Earth.

Finally, very low erosion rates for geomorphic surfaces along the Spirit traverse (0.03 nm per year)<sup>1</sup> attest to the slow rates of cracking that must occur in observed Mars rocks compared with Earth, because there are still large rocks present on these extremely old surfaces. In addition to the lower expected amplitude of Martian stresses relative to Earth's, these slow rates are likely also due to the lack of water which, through a variety of processes, propagates fractures at higher rates, see, for example, refs 45,56. Nevertheless, the size, and variance in the size, of rocks in the cratered plains of Gusev notably decreases with lower measured thermal inertia<sup>1</sup>, a proxy for the age of the surface where younger surfaces have higher thermal inertia. This trend is similar to the diminution of boulder size on surfaces of increasing age observed in desert pavements in arid environments on Earth where, through time, poorly sorted gravel-boulder dominated surfaces mechanically weather without significant transport into well-sorted 1–3 cm size pebbles, see, for example, refs 57,58. Thus, the observation that exposed Mars rocks get

smaller through time suggests that when surfaces are not buried by sand, thermal stress weathering processes on Mars ultimately result in a distribution of broken rocks similar to those observed in desert pavements of Earth, albeit at a slower rate. All of these observations point to the potential long-term importance of insolation in mechanical weathering processes acting on both of these terrestrial planets.

## Methods

**Collecting crack data from MER data products.** The MER Spirit and Opportunity missions have derived numerous data products from the Martian surface which are accessible on the internet (<http://an.rsl.wustl.edu/mer/>). In particular, 1,024 × 1,024 pixel stereo images collected by mission PANCAMs<sup>59</sup> are merged by NASA to create associated 3D data files. These files are composed of georeferenced xyz coordinates that represent the scene visible in the PANCAM 2D images, providing the data from which geometric measurements of the Martian surface may be made (summarized in Supplementary Methods). As of the time of publication, however, there had been no means by which to readily derive distance or orientation data from these data products.

We developed software, 'ImageRover,' (<http://visionlab.uncc.edu/index.php/mer-imagerover-app>), to provide an interface for visualization and geometric analysis of NASA's MER PANCAM 3D data products (Supplementary Fig. 1; Supplementary Methods). ImageRover employs MER mission 2D and 3D data directly from their publicly available repository (for example, NASA's Planetary Data System; [http://pdsimg.jpl.nasa.gov/Atlas/MER/mer1po\\_0xxx/data/](http://pdsimg.jpl.nasa.gov/Atlas/MER/mer1po_0xxx/data/)) and renders views of the Martian surface that enable user-friendly extraction of measurements. Specifically, a user is able to measure (1) point-to-point lengths between user-defined end-points and (2) orientations of user-defined planes (Supplementary Fig. 1). Crack plane azimuth orientations (strike) are expressed relative to Mars north–south–east–west (0–359°) and crack plane slope (dip) is expressed relative to horizontal (0–90°) in the same way that a geologist would report a right-hand rule strike and dip on Earth. All results published in this article are compiled from data available before July 2013 which include 29,714 EFF/XYZ stereoscopic images from the Spirit rover recorded during sols 1–2,209 (the entire mission).

To validate the accuracy of ImageRover calculations made from the MER data products, we compared crack length and strike and dips measured on 3D data of Earth boulders using ImageRover to the same measurements made using a tape measure and a compass in the field (Supplementary Fig. 2, Supplementary Table 1, Supplementary Methods). Overall, the differences between the measurements made using ImageRover and the same measurements made in the field were found to fall within errors associated with making the measurements with a compass. For example, the difference between measured biaxial strikes on individual cracks using the two methods are comparable to reported errors associated with making these measurements in the field alone; that is, ~9° for steeply dipping beds to ~30–50° for shallowly dipping beds<sup>60</sup>. Thirty-two per cent of the dip directions measured using ImageRover were opposite of that measured in the field particularly for high- and low-angle dips (Supplementary Methods), rendering strikes measured using the right-hand rule off by ±180° in Supplementary Table 1, but within the stated errors above when considered as biaxial data.

**Mars rock and crack measurements overview.** Using our software and MER Spirit data, we examined cracks on 1,573 rocks in total from 59 different sites along the Spirit traverse (Fig. 3), which comprises a range of volcanic rock types and geomorphic surfaces<sup>61</sup>. For all data collected, we examined only larger rocks (>10 and >20 cm) within a similar field of view within the image (that is, far distant rocks visible in images were avoided) to ensure good visibility of as many cracks as possible on rock surfaces. Also, to avoid thermal complexities associated with slope aspect or topography-induced shading<sup>13</sup>, we avoided collecting data on visibly significant ground slopes or immediately adjacent to significant topography. To avoid making measurements on tectonically induced fractures, all data were collected for individual boulders; no data were collected for bedrock outcrops. Although it has been suggested that solar-induced directional cracking may vary with latitude<sup>22,25</sup>, we limited our sampling to the Spirit traverse which, at the time of data collection, had overall larger numbers of data products with images of rocks that fit our sampling criteria.

Cracks were defined as any narrow lineation of pixels that strongly contrasted with adjacent features within a rock mass (Fig. 1). To minimize any bias in visualization of cracks of certain orientations due to shadowing effects, the time of day of all images employed in the study was limited to mid-day hours (~10:00 to ~15:00 hours) when the sun would be relatively high overhead (Supplementary Methods).

To produce a data set of crack orientations that were free from sampling bias associated with observation direction, we took advantage of observed relationships between image orientations and crack orientations. We first analysed the data set and our methods for potential sampling bias by measuring crack strikes and dips in 133 rocks using ImageRover. The results of this analysis (above), combined with the extremely time intensive nature of searching for, and analysing, appropriate

rocks with sufficiently complete 3D data available, led us to the development of methods specifically aimed at maximizing the numbers of rocks analysed while minimizing all sampling bias inherent to the Spirit data products (see below). Finally 1,440 rocks and their associated cracks were visualized in ImageRover and analysed for crack orientations.

**Identifying sampling bias potential for Spirit data products.** To characterize potential sampling biases that might arise from making field measurements using MER Spirit PANCAM data products, we collected a preliminary data set of rock and crack data (Supplementary Methods for details; Supplementary Data set 1). In 36 randomly selected MER Spirit sites, we randomly selected 76 images for which we used ImageRover software to measure the length and strike and dip of all visible cracks found in all imaged rocks that were > 10 cm in diameter (Supplementary Data set 1). The size of these analysed cracked rocks ranged from 10 cm to ~4 m with an average size of  $0.6 \pm 0.7$  m; however, our validation tests (Supplementary Methods) indicated that this average likely speaks to crack visibility in large rocks more than to the average size of a cracked rock. Thus crack data from Martian rocks are necessarily derived from a population of relatively large rocks compared with the compilation of similar data from Earth (Supplementary Data set 2).

Our analysis of randomly chosen images along the Spirit traverse also revealed a strong directional sampling bias of MER Spirit data products due to Spirit's predilection towards recording images in particular directions relative to the motion of the Rover. Specifically, the vast majority of Spirit images for which 3D data are available were recorded when the PANCAMS were pointing either in the direction of the motion of the rover (image azimuth = SE) or directly behind the rover (image azimuth = NW). Thus, the azimuths of any group of randomly selected images such as those chosen for our preliminary analysis (Fig. 4a) reflect this bias.

Another expected bias in the Spirit data set relates to the visibility of cracks of varying locations on the rock and orientations with respect to the orientation of the camera or viewer. In our field validation tests on boulders in North Carolina, USA, we noted that sunlit-rock-face-cracks having orientations oblique, or parallel to, the viewpoint of a distant observer (3–5 m) were less clear, or not visible at all, compared with cracks on rock faces oriented normal to the viewpoint of the observer.

We noted that this disparity in crack visibility transfers to 2D images and results in a smaller count, using our criteria, of those cracks that strike unfavourably relative to the azimuth orientation of the image. In particular, cracks that strike parallel to a 2D image (normal to the camera orientation) are overall less visible in any given image compared with those that strike into, and out of, the image for a combination of reasons. First, if they are vertical or subvertical, image-parallel-striking cracks will likely not be exposed in any rock face that is parallel to the image azimuth itself, giving such cracks a much lower chance of being observed. Furthermore, since the majority of these image-parallel/viewer normal-striking cracks will be located on rock faces that are oblique to the orientation of the photo, they have a much higher likelihood of being obscured by the protruding portions of the rock itself unless the rock is perfectly spherical. Such an obscuration would be particularly relevant to the MER data set and for the blocky, irregular rocks of the Martian surface because (1) any rock protrusion would reduce the contrast and/or consistent linear visibility for cracks located on the side of the rock behind the protrusion and/or (2) such protrusions would result in a hole in the 3D data where the crack is located behind them. Both of these outcomes would preclude measuring these image-parallel-striking cracks, because we defined cracks as any continuous lineation that starkly contrasted with adjacent pixels. Furthermore measurements can only be made on a feature if 3D data are complete in the area of interest. As a result, the majority of any measurable cracks in a given image will be striking in and out of the image itself. Analysis of the orientations of the 222 ImageRover-measured crack strikes and dips visible in the 133 rocks confirmed that the measured crack strikes were typically nearly equal to the image azimuth (Fig. 4b,c).

**Mars crack data collection.** Starting at MER Spirit site 2, we examined all images in order of the data product file listing via JPL. We searched for images that met the following criteria in order of image azimuth bin from 0 to 360° via 10° bins: only images with similar clarity of rock detail in the 2D and 3D images (that is, similar focal lengths in the bottom half of the image) and relatively level visible foreground surface were chosen. As such, we ensured that all the data were collected from images of comparable resolution and visual distance. If such an image was not available for the necessary 10° bin orientation at the chosen site, we went on to the next site. As such, we employed a stratified sampling strategy to select a random representation of differently oriented images along the Spirit Traverse (Figs 3 and 5 and Supplementary Data set 3).

For each selected image, a 50-box grid overlay provided a random reference from which to select rocks. The closest rocks greater than 20 cm diameter to each of the bottom 10 grid line intersections were chosen (Supplementary Fig. 3). If no rock was present at an interval, that interval was skipped, and we looked for the closest rock to the next grid point. All the above steps were repeated until we had identified 10 rocks from a suite of images that all fell within a given 10° image azimuth bin. We then moved on to the next azimuth bin and repeated the image/rock selection process starting with whichever site and image we had ended on

previously. We repeated these steps four times per 10° image azimuth bin for a total of 40 rocks per bin and 1,440 total rocks from 31 different sites along the Spirit traverse.

Finally, for each of these 1,440 rocks, we counted the total number of cracks visible in each rock using the criteria defined above. If a rock exhibited no cracks, then it was assigned a '0'. As such, we counted the total number of cracks per rock visible in typical large boulders on the Martian surface. The statistically robust correlation between crack and image orientation, combined with the equally distributed azimuths of the 1,440-rock images, enabled the confident use of image azimuth as a proxy for the orientation of any visible cracks in the image (Fig. 4; main text). Therefore, for each crack counted, we assigned it an orientation equal to the orientation of the image that it was found in (Fig. 6). We also plotted the image orientation for all rocks (565 of the 1,440) that did not exhibit visible cracks (Fig. 6d).

**Earth desert crack data compilation.** We compiled all available crack strike ( $n = 4,805$ ) and dip ( $n = 3,215$ ) data that we could find for surface boulders in Earth's deserts<sup>22–25,62</sup> (Fig. 2 and Supplementary Data set 2). Crack dip data were collected for only two of these studies<sup>23,62</sup>. If raw data were not available in the published work, we obtained the data from the first author directly. From each study, we included all the crack data available in our compilation. We did not attempt to account for rock type, anisotropies, surface age or other possible variables that would influence crack properties. As such, the data set comprises a variety of rock sizes (from ~1 cm to ~2 m) from a variety of desert locations ranging from about 40°N latitude to 30°S latitude. The majority of crack data is derived from study sites in the southwestern United States<sup>22,23,25,62</sup>, with about 450 cracks from the eastern Libyan Plateau in Egypt<sup>24</sup> and about 150 cracks from the Gobi and Strzelecki deserts<sup>22</sup>. Thus, most, but not all, data are from the northern hemisphere. Rock types included basalt, intrusive igneous rocks, meta-volcanic and meta-sedimentary rocks, carbonates and, to a lesser extent, clastic sedimentary rocks. In all studies, individual boulders (no bedrock data are reported) were chosen using selected spacing intervals, designated areas on specified geomorphic surfaces, and/or certain size criteria. Crack orientation data were collected on each selected boulder. For some studies<sup>24,25</sup>, only one orientation measurement was reported for all parallel cracks on an individual boulder. Thus, about one-fourth of the compiled data set might be underreporting certain orientations in the context of 'all cracks'. The minimum size boulder examined, as well as the minimum length of crack measured, varied somewhat for each of the studies, with a cutoff of 5 cm for rocks and 2 cm for cracks for the majority of the data. Rock size data are included in the compilation if available.

**Mars solar-induced thermal stress model.** In this study, we utilized the model employed by Molaro *et al.*<sup>38</sup> to simulate grain-scale thermoelastic stresses produced on Martian surfaces. This model is composed of two parts: a one-dimensional thermal model that calculates the temperatures in a macroscopic column of material throughout the solar day on a given body, and a 2D finite-element model<sup>63</sup>, which calculates thermoelastic deformation in a microstructure over the same period. The thermal model is used to calculate time-dependent solar and conductive heat fluxes at the surface and some depth, which can then be applied as boundary conditions in the 2D model, which uses those heat fluxes to calculate thermoelastic deformation over time. The idea behind coupling these two models together is that the 2D model investigates a 'zoomed in' version of the thermal model.

The original study did not include the effects of an atmosphere, and thus had to be modified for our purposes to make calculations for rocks on the Martian surface. It solves the heat equation, which is given by:

$$c_p \rho \frac{dT}{dt} + \nabla Q = 0 \quad (1)$$

where  $c_p$  is the specific heat capacity,  $\rho$  is the density,  $T$  is the temperature,  $k$  is the thermal conductivity and  $Q$  is the heat flux. Following the example of Aharonson and Schorghofer<sup>64</sup>, we included terms for atmospheric extinction (2), emission (3) and scattering (3) for a flat surface:

$$Q_{\text{sol}} = \frac{S}{R^2} (1 - A) e^{\frac{-\tau}{\cos(\theta)}} \quad (2)$$

$$Q_{\text{IR}} = f_{\text{IR}} \frac{S}{R^2} \sin(\theta_{\text{noon}}) \quad (3)$$

$$Q_{\text{scat}} = \frac{1}{2} f_{\text{scat}} \frac{S}{R^2} \quad (4)$$

where  $S$  is the solar constant,  $R$  is the solar distance,  $A$  is the albedo and  $\theta$  is the solar elevation angle.  $\tau$  is the optical depth at the Martian surface, which is taken to be 0.2 (refs 65,66). The extinction term (1) is proportional to the path length through the atmosphere, except at times of the day when it is limited by the radius of curvature of the planet. The emission term (2) approximates the atmospheric radiation as a fraction of the noontime solar insolation, and is kept constant throughout the day. The scattering term (4) assumes that half of the scattered light is lost to space. The emission factor ( $f_{\text{IR}}$ ) has a value of 0.04, and the scattering

factor ( $f_{\text{scat}}$ ) has a value of 0.02. We refer the reader to Aharonson and Schorghofer<sup>64</sup> for additional details on this model. We calculated the temperature of a Martian surface over one solar day during the warmest day of the year ( $L_s$  68) at a longitude of 0° and a latitude of 15°S.

The 2D model used was Finite Element Analysis of Microstructures (OOF2)<sup>65</sup>, a finite-element modelling programme designed to help scientists simulate the behaviour of microstructures. OOF2 calculates (1) and the force-balance (2) equation, given by:

$$M \frac{d^2 u}{dt^2} + \nabla \cdot \sigma = 0 \quad (5)$$

where  $M$  is the mass density tensor,  $u$  is the displacement field and  $\sigma$  is the stress tensor. It utilizes the time-dependent heat flux from the thermal model as boundary conditions to calculate stresses over one solar day. Additional details on this model can be found in Molaro *et al.*<sup>38</sup>, as we did not make any modifications to what was used in their original study. The microstructure modelled can be thought of as a small piece in an infinite half-space, where its top represents a surface open to space, the bottom represents 5 mm in depth. While the temperature was set to be periodic across horizontal boundaries, the displacement across horizontal boundaries is fixed. In this sense, the stresses cannot be directly compared with those calculated for boulders, as this model does not include the effects of boulder shape or surface curvature. We used a randomized grid of hexagons, each of which represents a pyroxene (75% of the total) or plagioclase (25% of the total) grain with a diameter of 360 microns. This composition approximates basaltic rock, which is abundant along the Spirit traverse. Values for the material parameters can be found in the Supplementary Table 2.

The stress parameter presented herein is the von Mises stress ( $\sigma_e$ , also sometimes called the equivalent stress. It is calculated from the principal stresses:

$$\sigma_e = \sqrt{\frac{(\sigma_1 - \sigma_2)^2 + (\sigma_2 - \sigma_3)^2 + (\sigma_1 - \sigma_3)^2}{2}} \quad (6)$$

Because the top of the microstructure is a free surface, most of the stress induced in our microstructure is along the  $x$  axis ( $\sigma_e \approx |\sigma_{xx}|$ ). Note that while  $\sigma_e$  always has a positive value, an artificial sign correction has been applied to Fig. 7 to visually separate the tensile and compressional regimes modelling.

## References

- Golombek, M. *et al.* Geology of the Gusev cratered plains from the Spirit rover traverse. *J. Geophys. Res.-Planet.* **111**, 1–27 (2006).
- Thomas, M., Clarke, J. & Pain, C. Weathering, erosion and landscape processes on Mars identified from recent rover imagery, and possible Earth analogues. *Aust. J. Earth Sci.* **52**, 365–378 (2005).
- Grant, J. *et al.* Surficial deposits at Gusev crater along Spirit rover traverses. *Science* **305**, 807–810 (2004).
- Ollier, C. *Weathering* (Longman Group, 1984).
- Larsen, I. J. *et al.* Rapid soil production and weathering in the Southern Alps, New Zealand. *Science* **343**, 637–640 (2014).
- Yokoyama, T. & Matsukura, Y. Field and laboratory experiments on weathering rates of granodiorite: separation of chemical and physical processes. *Geology* **34**, 809–812 (2006).
- Kirchner, J. W., Riebe, C. S., Ferrier, K. L. & Finkel, R. C. Cosmogenic nuclide methods for measuring long-term rates of physical erosion and chemical weathering. *J. Geochem. Explor.* **88**, 296–299 (2006).
- Millot, R., Gaillardet, J., Dupré, B. & Allègre, C. J. The global control of silicate weathering rates and the coupling with physical erosion: new insights from rivers of the Canadian Shield. *Earth Planet. Sci. Lett.* **196**, 83–98 (2002).
- Ashley, J. W. *et al.* Evidence for mechanical and chemical alteration of iron-nickel meteorites on Mars: process insights for Meridiani Planum. *J. Geophys. Res.-Planet.* **116**, 1–22 (2011).
- Jagoutz, E. Salt-induced rock fragmentation on Mars: the role of salt in the weathering of Martian rocks. *Adv. Space Res.* **38**, 696–700 (2006).
- Chan, M. A., Yonkee, W. A., Netoff, D. I., Seiler, W. M. & Ford, R. L. Polygonal cracks in bedrock on Earth and Mars: implications for weathering. *Icarus* **194**, 65–71 (2008).
- Clarke, J. in *Arid Zone Geomorphology: Process, Form and Change in Drylands* 3rd edn (ed. Thomas, D. S. G.) 61–82 (Wiley-Blackwell, 2011).
- Leask, H. & Wilson, L. in *34th Annual Lunar Planet. Sci. Conf.* 1320 (Houston, TX, USA, 2003).
- Delbo, M. *et al.* Thermal fatigue as the origin of regolith on small asteroids. *Nature* **508**, 233–236 (2014).
- Molaro, J. & Byrne, S. Rates of temperature change of airless landscapes and implications for thermal stress weathering. *J. Geophys. Res.-Planet.* **117**, E10011 (2012).
- Viles, H. *et al.* Simulating weathering of basalt on Mars and Earth by thermal cycling. *Geophys. Res. Lett.* **37**, L18201 (2010).
- Hall, K. & Thorn, C. E. Thermal fatigue and thermal shock in bedrock: an attempt to unravel the geomorphic processes and products. *Geomorphology* **206**, 1–13 (2014).
- Warren, K., Eppes, M.-C., Swami, S., Garbini, J. & Putkonen, J. Automated field detection of rock fracturing, microclimate, and diurnal rock temperature and strain fields. *Geosci. Instrum. Method. Data Syst.* **3**, 371–406 (2013).
- McKay, C. P., Molaro, J. L. & Marinova, M. M. High-frequency rock temperature data from hyper-arid desert environments in the Atacama and the Antarctic dry valleys and implications for rock weathering. *Geomorphology* **110**, 182–187 (2009).
- Gómez-Heras, M., Smith, B. J. & Fort, R. Surface temperature differences between minerals in crystalline rocks: implications for granular disaggregation of granites through thermal fatigue. *Geomorphology* **78**, 236–249 (2006).
- Hall, K. The role of thermal stress fatigue in the breakdown of rock in cold regions. *Geomorphology* **31**, 47–63 (1999).
- Eppes, M. C., McFadden, L. D., Wegmann, K. W. & Scuderi, L. A. Cracks in desert pavement rocks: further insights into mechanical weathering by directional insolation. *Geomorphology* **123**, 97–108 (2010).
- Eppes, M. *et al.* in *AGU Fall Meeting Abstracts* 0745 (San Francisco, CA, USA, 2010).
- Adelsberger, K. A. & Smith, J. R. Desert pavement development and landscape stability on the Eastern Libyan Plateau, Egypt. *Geomorphology* **107**, 178–194 (2009).
- McFadden, L., Eppes, M., Gillespie, A. & Hallet, B. Physical weathering in arid landscapes due to diurnal variation in the direction of solar heating. *Geol. Soc. Am. Bull.* **117**, 161–173 (2005).
- Shi, J. *Study of Thermal Stresses in Rock Due to Diurnal Solar Exposure* (MS thesis, University of Washington, 2011).
- Schorghofer, N. Temperature response of Mars to Milankovitch cycles. *Geophys. Res. Lett.* **35**, L18201 (2008).
- Forget, F., Haberle, R., Montmessin, F., Levrard, B. & Head, J. Formation of glaciers on Mars by atmospheric precipitation at high obliquity. *Science* **311**, 368–371 (2006).
- Laskar, J. *et al.* Long term evolution and chaotic diffusion of the insolation quantities of Mars. *Icarus* **170**, 343–364 (2004).
- Anderson, T. L. *Fracture Mechanics: Fundamentals and Applications* (CRC press, 2005).
- Atkinson, B. K. *Fracture Mechanics of Rock* (Academic Press, 1987).
- Atkinson, B. K. Subcritical crack growth in geological materials. *J. Geophys. Res.-Solid Earth* **89**, 4077–4114 (1984).
- Goudie, A. S. & Viles, H. A. The thermal degradation of marble. *Acta Univ. Carol. Geogr.* **35**, 7–16 (2000).
- Hall, K. Natural building stone composed of light-transmissive minerals: Impacts on thermal gradients, weathering and microbial colonization. A preliminary study, tentative interpretations, and future directions. *Environ. Earth Sci.* **62**, 289–297 (2011).
- Hall, K., Meiklejohn, I., Sumner, P. & Arocena, J. Light penetration into Clarens sandstone and implications for deterioration of San rock art. *Geoarchaeology* **25**, 122–136 (2010).
- Holzhausen, G. R. Origin of sheet structure, 1. Morphology and boundary conditions. *Eng. Geol.* **27**, 225–278 (1989).
- Molaro, J. & Byrne, S. in *44th Lunar Planet. Sci. Conf.* 1790 (Arizona, USA, 2013).
- Molaro, J. & Byrne, S. Grain-scale thermoelastic stresses and spatiotemporal temperature gradients on airless bodies, implications for rock breakdown. *J. Geophys. Res.-Planet.* **120**, 255–277 (2015).
- Molaro, J. & Byrne, S. *Thermoelastic Grain-Scale Stresses on Airless Bodies and Implications for Rock Breakdown #46* (American Astronomical Society, DPS meeting, 2014).
- Mellon, M. T. Small-scale polygonal features on Mars: seasonal thermal contraction cracks in permafrost. *J. Geophys. Res.-Planet.* **102**, 25617–25628 (1997).
- Mellon, M. T., Jakosky, B. M., Kieffer, H. H. & Christensen, P. R. High-resolution thermal inertia mapping from the Mars global surveyor thermal emission spectrometer. *Icarus* **148**, 437–455 (2000).
- Ferguson, R. L., Christensen, P. R. & Kieffer, H. H. High-resolution thermal inertia derived from the Thermal Emission Imaging System (THEMIS): thermal model and applications. *J. Geophys. Res.-Planet.* **111**, E12004 (2006).
- Edwards, C., Bandfield, J., Christensen, P. & Ferguson, R. Global distribution of bedrock exposures on Mars using THEMIS high-resolution thermal inertia. *J. Geophys. Res.-Planet.* **114**, E11001 (2009).
- Sumner, P., Nel, W. & Hedding, D. Thermal attributes of rock weathering: zonal or azonal? A comparison of rock temperatures in different environments. *Polar Geogr.* **28**, 79–92 (2004).
- Kranz, R. L. Microcracks in rocks: a review. *Tectonophysics* **100**, 449–480 (1983).
- Ersoy, A. & Atici, U. Performance characteristics of circular diamond saws in cutting different types of rocks. *Diam. Relat. Mater.* **13**, 22–37 (2004).
- Amitrano, D. & Helmstetter, A. Brittle creep, damage, and time to failure in rocks. *J. Geophys. Res.-Solid Earth* **111**, B11201 (2006).

48. Zhao, Y. Crack pattern evolution and a fractal damage constitutive model for rock. *Int. J. Rock Mech. Min. Sci.* **35**, 349–366 (1998).
49. Nara, Y. & Kaneko, K. Sub-critical crack growth in anisotropic rock. *Int. J. Rock Mech. Min. Sci.* **43**, 437–453 (2006).
50. Widhalm, C., Tschegg, E. & Eppensteiner, W. Anisotropic thermal expansion causes deformation of marble claddings. *J. Perform. Constr. Fac.* **10**, 5–10 (1996).
51. Tanigawa, Y. & Takeuti, Y. Three-dimensional thermoelastic treatment in spherical region and its application to solid sphere due to rotating heat source. *J. Appl. Math. Mech./Z. Angew. Math. Mech.* **63**, 317–324 (1983).
52. Hall, K. & André, M.-F. New insights into rock weathering from high-frequency rock temperature data: an Antarctic study of weathering by thermal stress. *Geomorphology* **41**, 23–35 (2001).
53. Batschelet, E. *Circular Statistics in Biology* Vol. 371 (Academic Press, 1981).
54. Molaro, J. L. & McKay, C. P. Processes controlling rapid temperature variations on rock surfaces. *Earth Surf. Proc. Land.* **35**, 501–507 (2010).
55. Greeley, R. *et al.* Wind-related processes detected by the Spirit rover at Gusev Crater, Mars. *Science* **305**, 810–813 (2004).
56. Moores, J. E., Pelletier, J. D. & Smith, P. H. Crack propagation by differential insolation on desert surface clasts. *Geomorphology* **102**, 472–481 (2008).
57. Mushkin, A., Sagy, A., Trabelci, E., Amit, R. & Porat, N. Measuring the time and scale-dependency of subaerial rock weathering rates over geologic time scales with ground-based lidar. *Geology* **42**, 1063–1066 (2014).
58. McFadden, L. D., Ritter, J. B. & Wells, S. G. Use of multiparameter relative-age methods for age estimation and correlation of alluvial fan surfaces on a desert piedmont, eastern Mojave Desert, California. *Quat. Res.* **32**, 276–290 (1989).
59. Bell, J. *et al.* Mars exploration rover Athena panoramic camera (PANCAM) investigation. *J. Geophys. Res.-Planet.* **108**, 8063 (2003).
60. Cruden, D. & Charlesworth, H. Errors in strike and dip measurements. *Geol. Soc. Am. Bull.* **87**, 977–980 (1976).
61. Crumpler, L. *et al.* Mars exploration Rover geologic traverse by the Spirit rover in the plains of Gusev crater, Mars. *Geology* **33**, 809–812 (2005).
62. Doyle, S. *Remotely Mapping Surface Roughness on Alluvial Fans: an Approach for Understanding Depositional Processes* (MS thesis, Univ. New Mexico, 2013).
63. Langer, S. A., Fuller, Jr E. R. & Carter, W. C. OOF: image-based finite-element analysis of material microstructures. *Comput. Sci. Eng.* **3**, 15–23 (2001).
64. Aharonson, O. & Schorghofer, N. Subsurface ice on Mars with rough topography. *J. Geophys. Res.-Planet.* **111**, E11007 (2006).
65. Vincendon, M., Langevin, Y., Poulet, F., Bibring, J. P. & Gondet, B. Recovery of surface reflectance spectra and evaluation of the optical depth of aerosols in the

near-IR using a Monte Carlo approach: application to the OMEGA observations of high-latitude regions of Mars. *J. Geophys. Res.-Planet.* **112**, E08S13 (2007).

66. Dundas, C. M. & Byrne, S. Modelling sublimation of ice exposed by new impacts in the Martian mid-latitudes. *Icarus* **206**, 716–728 (2010).
67. NASA. *Spirit Traverse Map (Sol 1506)*. Available at [http://mars.nasa.gov/mer/mission/tm-spirit/images/MERA\\_A1506\\_2\\_br2.jpg](http://mars.nasa.gov/mer/mission/tm-spirit/images/MERA_A1506_2_br2.jpg) (2008).

## Acknowledgements

The data presented in this paper are available in Supplementary Materials defined in the text. All MER data products depicted and employed are in the public domain and provided courtesy of NASA-JPL-CalTech; Planetary Data System. The ImageRover software used in this study is available at <http://visionlab.uncc.edu/index.php/mer-imagerover-app>. This work was funded by NASA ROSES Mars Data Analysis Program award # NNX09AI43G. We would like to thank Alan Gillespie and Les McFadden for helpful reviews of a previous version of this paper as well as the contributions of students Jennifer Aldred, Rebecca Adamick, and Jungphil Kwon. Dr Katherine Adelsberger generously provided unpublished raw data from her published work.

## Author contributions

The idea for this research, as well as the design, collection, analysis and interpretation of all MER data were completed or overseen by M.-C.E., who wrote the manuscript with input from A.W. and J.M. A.W., with M.-C.E.'s input, completed and/or oversaw the design and writing of ImageRover software. J.M. designed and wrote the numerical model presented and provided the majority of its interpretation within the manuscript. S.A. contributed to MER data collection and analysis. B.Z. contributed to ImageRover development.

## Additional Information

**Supplementary Information** accompanies this paper at <http://www.nature.com/naturecommunications>

**Competing financial interests:** The authors declare no competing financial interests.

**Reprints and permission** information is available online at <http://npg.nature.com/reprintsandpermissions/>

**How to cite this article:** Eppes, M.-C. *et al.* Cracks in Martian boulders exhibit preferred orientations that point to solar-induced thermal stress. *Nat. Commun.* 6:6712 doi: 10.1038/ncomms7712 (2015).